

# The orbital characters of bands in iron-based superconductor $\text{BaFe}_{1.85}\text{Co}_{0.15}\text{As}_2$

Y. Zhang, F. Chen, C. He, B. Zhou, B. P. Xie, and D. L. Feng\*

*State Key Laboratory of Surface Physics, Key Laboratory of Micro and Nano Photonic Structures (MOE),  
and Department of Physics, Fudan University, Shanghai 200433, People's Republic of China*

C. Fang, W. F. Tsai and J. P. Hu†

*Department of Physics, Purdue University, West Lafayette, Indiana 47907, USA*

X. H. Chen

*Department of Physics, University of Science and Technology of China,  
Hefei, Anhui 230027, People's Republic of China*

H. Hayashi, J. Jiang, H. Iwasawa, K. Shimada, H. Namatame, M. Taniguchi

*Hiroshima Synchrotron Radiation Center and Graduate School of Science,  
Hiroshima University, Hiroshima 739-8526, Japan.*

The unconventional superconductivity in the newly discovered iron-based superconductors is intimately related to its multi-band/multi-orbital nature. Here we report the comprehensive orbital characters of the low-energy three-dimensional electronic structure in  $\text{BaFe}_{1.85}\text{Co}_{0.15}\text{As}_2$  by studying the polarization and photon energy dependence of angle-resolved photoemission data. While the distributions of the  $d_{xz}$ ,  $d_{yz}$ , and  $d_{3z^2-r^2}$  orbitals agree with the prediction of density functional theory, those of the  $d_{xy}$  and  $d_{x^2-y^2}$  orbitals show remarkable disagreement with theory. Our results point out the inadequacy of the existing band structure calculations, and more importantly, provide a foundation for constructing the correct microscopic model of iron pnictides.

## I. INTRODUCTION

Unlike the cuprates, the low-energy electronic structure of the iron-based superconductors is dominated by multiple bands and orbitals [1–3]. Theoretically, it has been proposed that the Fermi surface sheets with multiple orbitals could result in a strong anisotropy and amplitude variation of the superconducting gaps [4, 5]. Experimentally, a recent study on  $\text{Ba}_{0.6}\text{K}_{0.4}\text{Fe}_2\text{As}_2$  shows that the superconducting gap sizes are different at the same Fermi momentum for two bands with different orbital characters [6]. To construct correct models for the iron-based superconductors, and to understand the unconventional superconductivity, it is thus critical to experimentally identify the orbital characters of the low-energy electronic structure.

There have been inconsistencies over the orbital identities of the bands amongst theories [2, 3], and a few experiments [7–12]. Moreover, various physical properties of iron-based superconductors are featured with three dimensional (3D) characters [13]. For example, the band structure in the so-called “122” series of iron-pnictides is rather 3D [10, 14], and the gap dependency on the out-of-plane momentum ( $k_z$ ) has recently been reported [6]. It has been pointed out that the three dimensionality of the electronic structure might be essential in inducing both the spin density wave (SDW) and superconductivity [15]. However, the orbital character distribution along the  $k_z$

direction in 3D momentum space has not been exposed so far.

Here we report a systematic angle-resolved photoemission spectroscopy (ARPES) study on the orbital character of the electronic structure in an electron-doped “122” compound,  $\text{BaFe}_{1.85}\text{Co}_{0.15}\text{As}_2$ . We have observed strong polarization dependency for all the bands near the Fermi energy ( $E_F$ ), and have obtained a comprehensive picture of the orbital characters of these bands. We confirm previous theoretical findings that the bands with  $d_{xz}$ ,  $d_{yz}$  orbital form two hole pockets around the zone center and one electron pocket around the zone corner, and the  $d_{3z^2-r^2}$  (or  $d_z$  for simplicity) orbital is mostly included in the two bands well below  $E_F$ . More importantly, we find that certain bands predicted to be of the  $d_{xy}$  orbital in theory are actually mixed with the  $d_{x^2-y^2}$  orbital around the zone center, and are dominated by the  $d_{x^2-y^2}$  orbital around the zone corner. Furthermore, we have identified the orbital characters of the band structure in 3D momentum space. Our results provide explicit knowledge for constructing the theoretical model of iron-based superconductors.

## II. POLARIZATION-DEPENDENT ARPES

$\text{BaFe}_{1.85}\text{Co}_{0.15}\text{As}_2$  single crystals were synthesized by a self-flux method [16] with a superconducting transition temperature ( $T_c$ ) of 25 K, and no SDW or structural transition. As this system is optimally doped with electrons, the low energy band structure is well occupied, and free from the complications of the electronic reconstruction in the SDW state [17–20]. Because the arsenic ions in

\*Electronic address: dlffeng@fudan.edu.cn

†Electronic address: hu4@purdue.edu

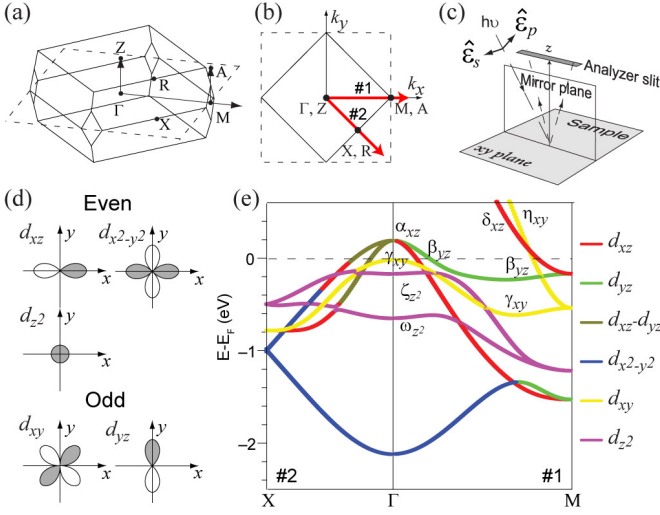


FIG. 1: (Color online) The experimental setup and definitions. (a) The Brillouin zone of  $\text{BaFe}_{1.85}\text{Co}_{0.15}\text{As}_2$ . (b) Two-dimensional plot of the simplified Brillouin zone (solid line) and the unfolded Brillouin zone (dashed line). (c) Experimental setup for polarization-dependent ARPES. For the  $p$  (or  $s$ ) experimental geometry, the electric field direction of the incident photons  $\hat{\epsilon}_p$  (or  $\hat{\epsilon}_s$ ) is parallel (or perpendicular) to the mirror plane defined by the analyzer slit and the sample surface normal. (d) Illustration of the spatial symmetry of the  $3d$  orbitals with respect to the mirror plane formed by surface normal and cut #1 in panel b, *i.e.* the  $xz$  plane. (e) A typical orbital assignment of bands of iron pnictide as calculated in Ref. [3].

the FeAs layer are situated in two inequivalent positions, there are two iron ions per unit cell. The Brillouin zone of  $\text{BaFe}_{1.85}\text{Co}_{0.15}\text{As}_2$  is shown in Figs. 1(a) and 1(b). To compare with theory, we define the  $k_x$  and  $k_y$  directions to be the Fe-Fe bond directions, as shown in the unfolded Brillouin zone (dashed lines) for one iron ion per unit cell. Two high symmetry directions,  $\Gamma(\text{Z})\text{-M}(\text{A})$  and  $\Gamma(\text{Z})\text{-X}(\text{R})$ , are illustrated by red arrows #1 and #2, respectively in Fig. 1(b).

The polarization-sensitivity of the orbitals in ARPES is a powerful tool to identify the orbital characters of band structure [21]. The matrix element of the photoemission process can be described by

$$|M_{f,i}^{\mathbf{k}}| \propto |\langle \phi_f^{\mathbf{k}} | \hat{\epsilon} \cdot \mathbf{r} | \phi_i^{\mathbf{k}} \rangle|^2$$

, where  $\hat{\epsilon}$  is the unit vector of the electric field of the light [21]. For high kinetic-energy photoelectrons, the final-state wavefunction  $\phi_f^{\mathbf{k}}$  can be approximated by a plane-wave state  $e^{i\mathbf{k}\cdot\mathbf{r}}$  with  $\mathbf{k}$  in the mirror plane as plotted in Fig. 1(c). Consequently, it is always even with respect to the mirror plane. For the  $p$  (or  $s$ ) experimental geometry in Fig. 1(c), because  $\hat{\epsilon}$  is parallel (or perpendicular) to the mirror plane,  $\hat{\epsilon} \cdot \mathbf{r}$  is even (or odd). Therefore, to have finite matrix element, *i.e.* to be observed, the initial state  $\phi_i^{\mathbf{k}}$  has to be even (or odd) in the  $p$  (or  $s$ ) geometry.

Considering the spatial symmetry of the  $3d$  orbitals

TABLE I: The possibility to detect  $3d$  orbitals along two high symmetry directions in the  $p$  and  $s$  geometry by polarization-dependent ARPES

High-symmetry direction	Experimental geometry	$3d$ orbitals				
		$d_{xz}$	$d_{x^2-y^2}$	$d_{z^2}$	$d_{yz}$	$d_{xy}$
#1 $\Gamma(\text{Z})\text{-M}(\text{A})$	$p$	✓	✓	✓		
	$s$				✓	✓
#2 $\Gamma(\text{Z})\text{-X}(\text{R})$	$p$	✓		✓	✓	✓
	$s$	✓	✓		✓	

[Fig. 1(d)], when the analyzer slit is along the high symmetry direction of the sample, the photoemission signal of certain orbitals would appear or disappear by specifying the polarization directions as summarized in Table I. For example, with respect to the mirror plane formed by direction #1 and sample surface normal (or the  $xz$  plane), the even orbitals ( $d_{xz}$ ,  $d_{z^2}$ , and  $d_{x^2-y^2}$ ) and the odd orbitals ( $d_{xy}$  and  $d_{yz}$ ) could be only observed in the  $p$  and  $s$  geometry respectively. Note that,  $d_{xz}$  and  $d_{yz}$  are not symmetric with respect to the mirror plane defined by direction #2 and surface normal, thus could be observed in both the  $p$  and  $s$  geometries.

Figure 1(e) shows the band calculation of iron-based superconductors in a two-dimensional (2D) band model reproduced from Ref.[3], which was confirmed by many other calculations, and widely adopted in various models. The bands are labeled with corresponding orbital characters as subscripts. Around the  $\Gamma$  point, the  $d_{z^2}$  orbital contributes to the two bands  $\zeta_{z^2}$  and  $\omega_{z^2}$  well below  $E_F$ . There are three holelike bands near  $E_F$ .  $\alpha_{xz}$  and  $\beta_{yz}$  cross  $E_F$  forming two hole pockets, while the band top of  $\gamma_{xy}$  is just below  $E_F$ . The  $\beta_{yz}$  and  $\gamma_{xy}$  disperse to the lower binding energies at M. Two bands,  $\delta_{xz}$  and  $\eta_{xy}$ , form two electron pockets, and they are degenerate with  $\beta_{yz}$  and  $\gamma_{xy}$  at M respectively. The  $d_{x^2-y^2}$  orbital was found to be irrelevant to the low-energy electronic structure.

ARPES measurements were performed at the Beamline 1 of Hiroshima synchrotron radiation center (HSRC). By rotating the the entire photoemission spectroscope around the incoming photon beam, one can switch between the  $s$  and  $p$  polarization geometries. All the data were taken with a Scienta electron analyzer at 30 K, the overall energy resolution is 15 meV, and the angular resolution is  $0.3^\circ$ . The sample was cleaved *in situ*, and measured under ultra-high-vacuum of  $5 \times 10^{-11}$  torr.

### III. RESULTS

#### A. Orbital characters of bands around the zone center

The photoemission data taken near the zone center are shown in Fig. 2. Two bands assigned as  $\zeta$  and  $\omega$  could

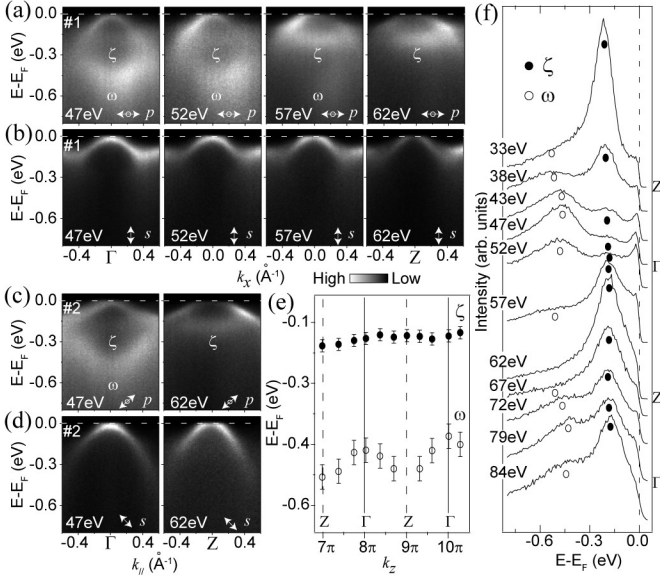


FIG. 2: Photoemission data around the zone center. (a) and (b), The photon energy dependence of the photoemission intensity  $[I(k, \omega)]$  along  $\Gamma(Z)$ -M(A) (#1) in the  $p$  and  $s$  geometries, respectively. (c) and (d), The photon energy dependence of  $I(k, \omega)$  along  $\Gamma(Z)$ -X(R) (#1) in the  $p$  and  $s$  geometries, respectively. (e) The  $k_z$  dispersion of the  $\zeta$  and  $\omega$  bands along  $\Gamma$ -Z. (f) The photon energy dependence of EDCs sampled along  $\Gamma$ -Z.

be observed at about 170 and 500 meV below  $E_F$ . Both bands only emerge in the  $p$  geometry, and could not be observed in the  $s$  geometry along both #1 and #2 directions [Figs. 2(a)-2(d)]. Based on Table I, these two bands are made of  $d_{z^2}$  orbital, assuming they are consisted of a single orbital as suggested in Fig. 1(e). The energy distribution curves (EDCs) at  $k_{\parallel} = 0 \text{ \AA}^{-1}$  taken with different photon energies are stacked in Fig. 2(f), so that we could track the  $\zeta$  and  $\omega$  bands along  $\Gamma$ -Z. The peak position of  $\omega$  shows a periodic variation if we take the inner potential to be 15 eV [Fig. 2(e)]. Furthermore, the peak intensities of  $\omega$  and  $\zeta$  show periodic anti-correlation with the photon energy. While  $\omega$  is at its strongest at  $\Gamma$  (47 and 79 eV),  $\zeta$  is mostly enhanced at Z (33 and 62 eV). The anti-correlation of intensities of these two bands could be naturally explained by the different wavefunction distributions along the  $z$  direction for the bonding and antibonding states formed by the  $d_{z^2}$  orbitals [22]. Summing up these facts, we attribute  $\zeta$  and  $\omega$  to  $d_{z^2}$  orbital, which agrees with the assignments in Fig. 1(e).

Near the Fermi energy, three bands ( $\alpha$ ,  $\beta$ , and  $\gamma$ ) could be identified around  $\Gamma$  in Fig. 3.  $\alpha$  only shows up in the  $p$  geometry, while  $\beta$  only appears in the  $s$  geometry, exhibiting opposite spatial symmetries [Figs. 3(a)-(e)]. The band tops of both  $\alpha$  and  $\beta$  are below  $E_F$  and degenerate at the  $\Gamma$  point. Note that the bands with  $d_{xz}$  and  $d_{yz}$  orbitals should be degenerate at the  $\Gamma$  point due to the four-fold symmetry of the sample. Therefore,

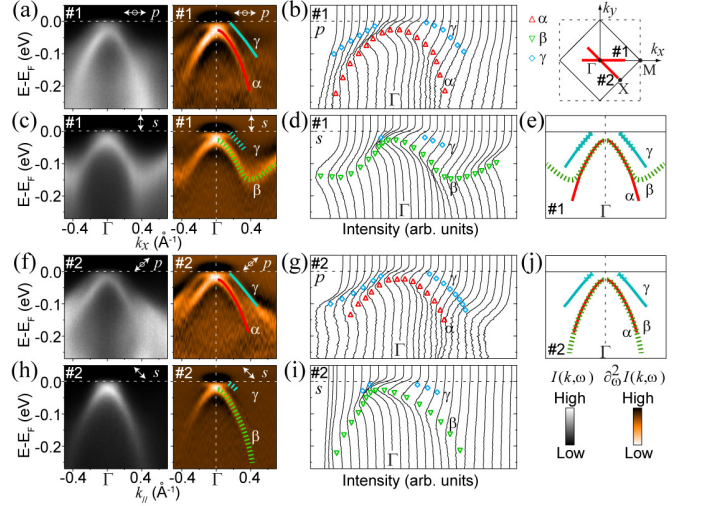


FIG. 3: (Color online) The polarization dependent APRES data around  $\Gamma$  taken with 47 eV photons. (a)  $I(k, \omega)$  map and its second derivative with respect to energy ( $\partial^2 I(k, \omega)/\partial \omega^2$ ) taken with the  $p$  geometry along #1 direction as marked with a red thick solid line in the inset. (b) The EDCs for the data in panel a. (c) and (d) are the same as panels a and b, but taken with the  $s$  geometry. (e) The sketch of the band structure in panels a and c. (f)-(j) are the same as (a)-(e), but taken along cut #2 in the inset. The band dispersions are identified with the help of second derivative image and EDCs, and illustrated by the solid and dashed lines plotted on the second derivative image. The color scale of  $I(k, \omega)$  and  $\partial^2 I(k, \omega)/\partial \omega^2$  are shown in the inset. The solid and dashed sketches of the bands represent the even and odd components of the bands respectively. These color scales and notations are compiled throughout the paper.

we attribute the  $\alpha$  and  $\beta$  bands to be of the  $d_{xz}$  and  $d_{yz}$  orbitals, respectively in this direction. In addition, along the  $\Gamma$ -M direction,  $\alpha$  disperses to the binding energy over 200 meV, and  $\beta$  disperses to about 150 meV and then bends over to lower binding energies toward the M point, which is consistent with the behavior of  $\alpha_{xz}$  and  $\beta_{yz}$  predicted by theory in Fig. 1(e). The  $d_{xz}$  and  $d_{yz}$  orbitals have no definite symmetry with respect to the  $\Gamma$ -X direction. The strong polarization dependence of  $\alpha$  and  $\beta$  observed along  $\Gamma$ -X direction [Figs. 3(f)-3(j)] are most likely due to the hybridization of the  $d_{xz}$  and  $d_{yz}$  orbitals. For example,  $\frac{d_{xz} + d_{yz}}{\sqrt{2}}$  and  $\frac{d_{xz} - d_{yz}}{\sqrt{2}}$  are of even and odd spatial symmetry with respect to the  $\Gamma$ -X direction, respectively. Actually, because of the four-fold symmetry, the  $d_{xz}$  component of  $\alpha$  along the  $k_x$  axis has to become  $d_{yz}$  along the  $k_y$ -axis. Therefore, the equal mixing of these two orbitals along the  $\Gamma$ -X direction is expected. Similar arguments hold for the  $\beta$  band.

The  $\gamma$  band could be observed in both geometries, indicating that it is a mixture of both odd and even orbitals. With respect to  $\Gamma$ -M, the odd orbital candidates are  $d_{xy}$  and  $d_{yz}$ . As the  $d_{yz}$  orbital contributes to  $\beta$ , the odd orbital in  $\gamma$  is likely  $d_{xy}$ , as the  $\gamma_{xy}$  band proposed in



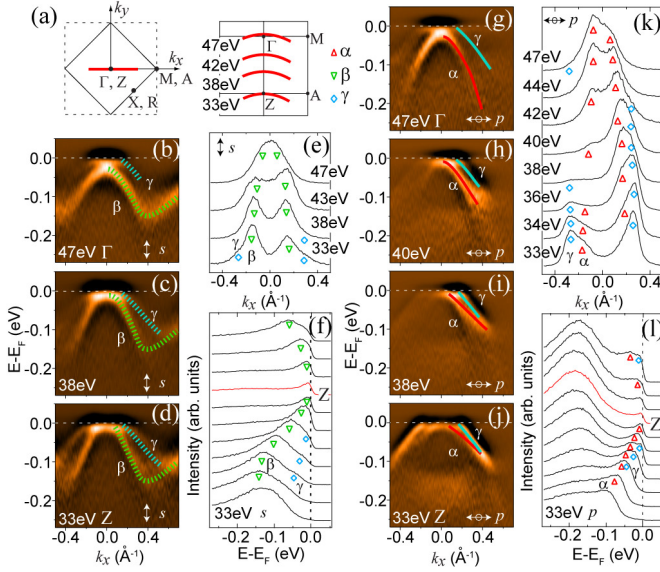


FIG. 4: (Color online) Photon energy dependence of bands near the zone center. (a) Illustration of the cuts sampled with different photon energies. (b)-(d)  $\partial^2 I(k, \omega) / \partial \omega^2$  taken in the  $s$  geometry with 47, 38 and 33 eV photons respectively. (e) The photon energy dependence of the MDCs at 30 meV below  $E_F$  in the  $s$  geometry. (f) The EDCs for the data in panel d. (g)-(j)  $\partial^2 I(k, \omega) / \partial \omega^2$  taken in the  $p$  geometry with 47, 40, 38 and 33 eV photons respectively. (k) The photon energy dependence of the MDCs at 30 meV below  $E_F$  in the  $p$  geometry. (l) The EDCs for the data in panel j.

Fig. 1(e). The even orbital candidates include  $d_{xz}$ ,  $d_{z^2}$  and  $d_{x^2-y^2}$ . Since  $\alpha$  ( $d_{xz}$ ),  $\zeta$  ( $d_{z^2}$ ), and  $\omega$  ( $d_{z^2}$ ) bands contains no odd orbital, the odd orbitals in  $\gamma$  are less likely mixed with the  $d_{xz}$  and  $d_{z^2}$  orbital in this momentum region. We thus deduce that the most possible even orbital in  $\gamma$  is  $d_{x^2-y^2}$ . Because both  $d_{xy}$  and  $d_{x^2-y^2}$  orbitals mainly spread in the FeAs plane, the  $\gamma$  band are expected to be more two dimensional than the  $\alpha$  and  $\beta$  bands. Such an assignment is consistent with the polarization dependence of data along  $\Gamma$ -X as well [Figs. 3(f)-3(j)], just  $d_{x^2-y^2}$  is the odd orbital, and  $d_{xy}$  is the even one in this direction.

To confirm such 2D nature of the  $\gamma$  band, and explore the 3D characters of the  $\alpha$  and  $\beta$  bands, photon energy dependent data around the zone center are shown in Fig. 4. The  $\beta$  band shifts away from the zone center when approaching the Z point [Figs. 4(b)-(d)], which is also illustrated by the shift of the momentum distribution curve (MDC) peaks of  $\beta$  in Fig. 4(e). The  $k_z$  dependence of the  $\alpha$  band shows similar behavior as  $\beta$ , with its band top below  $E_F$  at  $\Gamma$ , but slightly above  $E_F$  at Z [Figs. 4(g)-4(j)]. Moreover, the in-plane dispersion of  $\alpha$  becomes quite flat and eventually intersect the  $\gamma$  band around Z as shown in Figs. 4(j) and 4(l). The MDC peak positions of  $\gamma$  show almost no photon energy dependence in Fig. 4(k), and no obvious  $k_z$  influence on its in-plane dispersion is observed as well. Therefore, unlike

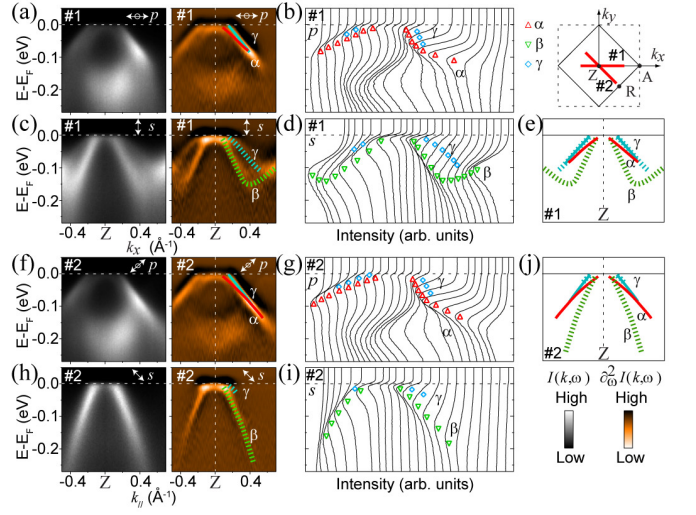


FIG. 5: (Color online) The polarization dependent APRES data around Z taken with 33 eV photons. (a)  $I(k, \omega)$  map and  $\partial^2 I(k, \omega) / \partial \omega^2$  taken with the  $p$  geometry along #1 direction as marked with a red thick solid line in the inset. (b) The EDCs for the data in panel a. (c) and (d) are the same as in panels a and b, but taken with the  $s$  geometry. (e) The sketch of the band structure in panels a and c. (f)-(j) are the same as in (a)-(e), but taken along #2 direction as marked with a red thick solid line in the inset.

the strong  $k_z$  dependence of  $\alpha$  and  $\beta$ , the weak  $k_z$  dependence of  $\gamma$  is consistent with the nature of  $d_{x^2-y^2}$  and  $d_{xy}$ , which are more in-plane than the other 3d orbitals. Note that,  $\gamma$  is more intensive in both polarization geometries near Z, likely due to matrix element effects related to its distribution along the crystallographic  $c$  axis.

The band structure and orbital characters around Z are shown in Fig. 5. The  $\alpha$  and  $\beta$  bands cross  $E_F$  along both the Z-A and Z-R directions, and thus form two hole pockets around the Z point. The polarization dependence of the spectra near Z are similar to that near  $\Gamma$ . Therefore, around the zone center, all the bands keep the same spatial symmetry at different  $k_z$ 's.

## B. Orbital characters of bands around the zone corner

The polarization dependent photoemission data around the zone corner are plotted in Fig. 6. The electron-like  $\delta$  band is degenerate with  $\beta$  at about 40 meV below  $E_F$  at M. The  $\delta$  band is much more pronounced in the  $p$  geometry, while  $\beta$  is very strong in the  $s$  geometry. On the other hand, some residual spectral weight of  $\beta$  could still be observed in the  $p$  geometry at M, and some infinitesimal  $\delta$  band spectral weight could be observed in the  $s$  geometry at both M and A, indicating a light mixing between  $\beta$  and  $\delta$ . If we assume that the orbital character of  $\beta$  does not change abruptly, its main composition can be then attributed to the odd  $d_{yz}$  orbital,

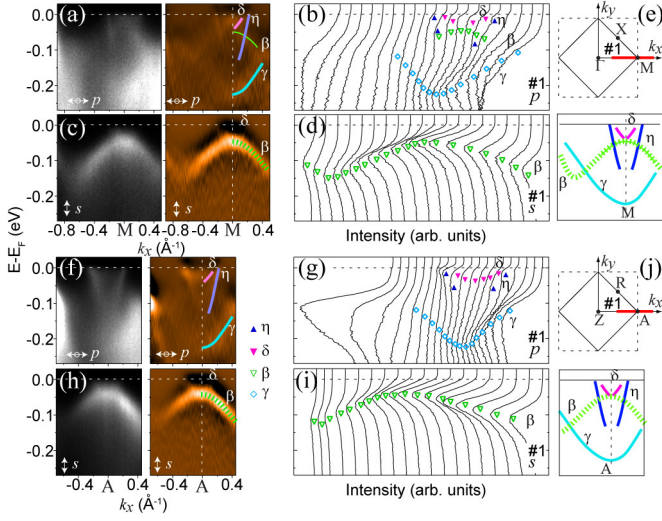


FIG. 6: (Color online) The polarization dependent APRES data around the zone corner. (a)  $I(k, \omega)$  and  $\partial^2 I(k, \omega)/\partial \omega^2$  map taken with the  $p$  geometry and 51 eV photons across M along the red thick line in the inset of panel e. (b) The EDCs for the data in panel a. (c) and (d) are the same as in panels a and b, but taken under the  $s$  geometry. (e) The sketch of the band structure in panels a and c. (f)-(j) are the same as in (a)-(e), but taken with 38 eV photons across A along the red thick line in the inset of panel j.

based on its  $d_{yz}$  orbital character around  $\Gamma$ . In Fig. 1(e), the  $\delta$  band is attributed to the even  $d_{xz}$  orbital, which is consistent with its mainly even character observed here.

The  $\eta$  band disperses over 150 meV below  $E_F$ , which is very close to the  $\gamma$  band at about -220 meV. This pair of bands ( $\gamma$  and  $\eta$ ) was previously predicted to be of  $d_{xy}$  with odd symmetry [Fig. 1(e)]. However surprisingly, both of them are actually even and only appear in the  $p$  geometry around the zone corner [Figs. 6(a) and 6(f)].

To further settle the orbital characters around the zone corner, Figs. 7(a)-7(f) shows the photoemission intensity map around the M and A point by rotating the sample azimuthally. Obviously, multiple disconnected parts of the Fermi surface are either enhanced or suppressed by the  $p$  or  $s$  geometries, which again demonstrates the multi-orbital nature of the Fermi surface. Although the polarization selection rules of different orbitals in Table I are not strict when the cuts are not exactly along the high symmetry direction, they still manifest themselves effectively, for example, as strong intensity modulations along Fermi surface sheets composed of sections with opposite spatial symmetries. Combining the Fermi surface parts observed in both the  $p$  and  $s$  geometries, one obtains two electron pockets around the M and A points [Figs. 7(c) and 7(f)]. The inner electron pocket is contributed by the  $\delta$  band. If we assume  $\delta$  to be the  $\delta_{xz}$  band along  $\Gamma$ -M in Fig. 1(e), its horizontal ( $k_x$ ) sections are made of the  $d_{xz}$  orbital, which could be thus observed in the  $p$  geometry [the red solid line in Figs. 7(a) and 7(d)]. Since the four-fold and translational symmetries of the crystal

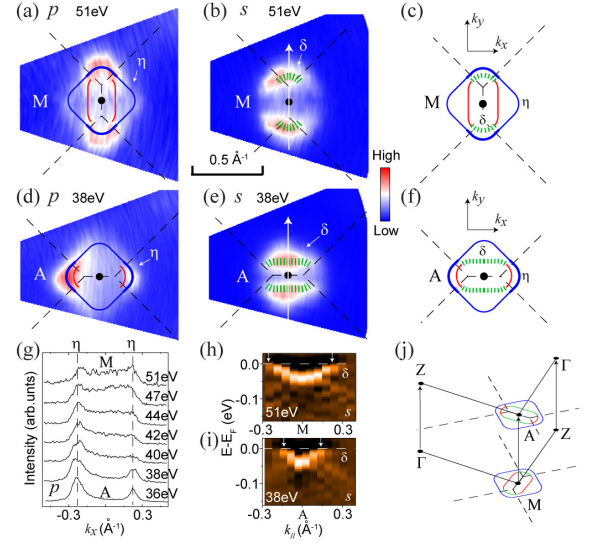


FIG. 7: (Color online) Fermi surface around the zone corner. (a) and (b) are the photoemission intensity maps taken with 51 eV photons around M in the  $p$  and  $s$  geometry respectively. (c) The sketch of the Fermi surface sheets observed in panels a and b. (d)-(f) are the same as in (a)-(c), but taken with 38 eV photons around A. (g) The photon energy dependence of the MDCs at  $E_F$  in the  $p$  geometry along the  $\Gamma$ (Z)-M(A) direction. (h) and (i)  $\partial^2 I(k, \omega)/\partial \omega^2$  map obtained by merging selected EDCs in the  $s$  geometry along the white arrows in panels b and e, respectively. (j) The illustration of the Fermi surface at A and M in the 3D Brillouin zone.

would result in the rotating distribution of the  $d_{xz}$  and  $d_{yz}$  orbitals, the vertical ( $k_y$ ) sections of  $\delta$  are made of the  $d_{yz}$  orbital, which could be thus observed in the  $s$  geometry [the green dashed line in Figs. 7(b) and (e)]. Moreover, the elliptical shape of the  $\delta$  pocket rotates  $90^\circ$  from M to A, which is consistent with the 3D character of the Brillouin zone [Fig. 7(j)]. As shown in Figs. 7(h) and 7(i), the distance between the two Fermi crossings of the  $\delta$  band along the vertical ( $k_y$ ) direction shrinks significantly from M to A. Therefore, the alternating even and odd orbital nature and strong  $k_z$  dependence of  $\delta$  electron pocket further supports its  $d_{xz}$  and  $d_{yz}$  orbital characters.

The outer square-like pocket, as shown by the blue solid line in Figs. 7(a) and 7(d), is from the  $\eta$  band. It is even and thus could be only observed in the  $p$  geometry. Among the three even orbitals, we could first exclude the  $d_{xz}$  orbital in the  $\eta$  pocket, otherwise, one would have observed the corresponding  $d_{yz}$  component of  $\eta$  along  $k_y$  in the  $s$  geometry, due to the four-fold symmetry of the sample. Furthermore, the  $\eta$  Fermi pocket is particularly intense in the Z-A or Z-M direction, as indicated by the thicker blue lines in Figs. 7(a) and 7(d). The rotation of these intense sections from A to M suggests the existence of orbital mixing rather than simple matrix element effect. Therefore, the  $\eta$  band should be the mixture of  $d_{x^2-y^2}$  and  $d_{z^2}$  orbitals. As shown in Fig. 7(g),

the peak intensity of  $\eta$  show asymmetry with respect to the A point. Similarly, in Fig. 7(d), the intense section of  $\eta$  in the first Brillouin zone is more intensive than that in the extended Brillouin zone on the right side. This contradicts the behavior of the  $d_{x^2-y^2}$  orbital, as the matrix element or photoemission intensity of  $d_{x^2-y^2}$  should become stronger as the in-plane momentum became larger. We thus conclude that the intense sections of  $\eta$  are consist of the  $d_{z^2}$  orbital over these momentum regions. On the other hand, considering the facts that the  $\eta$  electron pocket shows no  $k_z$  dependence as the corresponding MDCs peak positions do not change with the photon energies in Fig. 7(g), the  $\eta$  pocket is mostly made of the more in-plane  $d_{x^2-y^2}$  orbital.

The orbital assignment of the  $\eta$  pocket could naturally explain the orbital character of the  $\gamma$  band near the zone corner. Since  $\gamma$  is actually the same band as  $\eta$  in the unfolded Brillouin zone, they are thus degenerate and have the same orbital characters at M [2, 3]. Therefore, the  $\gamma$  band is also dominated by  $d_{x^2-y^2}$  at the zone corner (possibly some  $d_{z^2}$ ), which indicates that the  $d_{x^2-y^2}$  component of  $\gamma$  grows from  $\Gamma$  to M.

#### IV. DISCUSSION

Based on the above analysis, the orbital characters of the low-energy electronic structure of  $\text{BaFe}_{1.85}\text{Co}_{0.15}\text{As}_2$  are summarized in Fig. 8. The bands with  $d_{xz}$  and  $d_{yz}$  orbitals, including  $\alpha$ ,  $\beta$  and  $\delta$ , are well consistent with the band calculation in Fig. 1(e). The in-plane dispersion of the  $\alpha$  band varies much more strongly with  $k_z$  than that of the  $\beta$  band. This difference in the  $k_z$  dependencies between  $\alpha$  and  $\beta$  is consistent with the density function theory calculations in  $\text{BaFe}_2\text{As}_2$  [23] and previous ARPES studies [6, 14]. In particular, in the 3D model of  $\text{BaFe}_2\text{As}_2$  [15], the sizes of the hole pockets at Z are larger than that at  $\Gamma$ , which quantitatively agrees with our results as well. However, our experimental result seems not to support the orbital character change from Z-A to Z-R predicted in Ref.[15], which states that the  $\alpha$  and  $\beta$  would be correspondingly composed of  $d_{xy}$  and  $d_{x^2-y^2}$  orbital along the Z-R direction.

The most remarkable findings here are the orbital characters of the  $\gamma$  and  $\eta$  bands. They are dominated by the  $d_{x^2-y^2}$  orbital around the zone corner, and  $\gamma$  is a mixture of  $d_{xy}$  and  $d_{x^2-y^2}$  at the zone center. However, in most band calculations, the  $\gamma$  and  $\eta$  bands are proposed to be purely  $d_{xy}$ , and the  $d_{x^2-y^2}$  states are far from  $E_F$ . Our results disprove this picture. Furthermore, the band top of the  $\gamma$  band is found to be higher than those of the  $\alpha$  and  $\beta$  at the zone center, which is also inconsistent with the band calculations shown in Fig. 1(e). Considering the 2D character of the  $\gamma$  and  $\eta$  bands, the  $d_{xy}$  and  $d_{x^2-y^2}$  orbitals should interact less with states outside the Fe layer (such as As  $4p_z$  states) than the other 3d orbitals. Therefore, our results indicate that the energy of the  $d_{xy}$  and  $d_{x^2-y^2}$  orbitals may not be calculated cor-

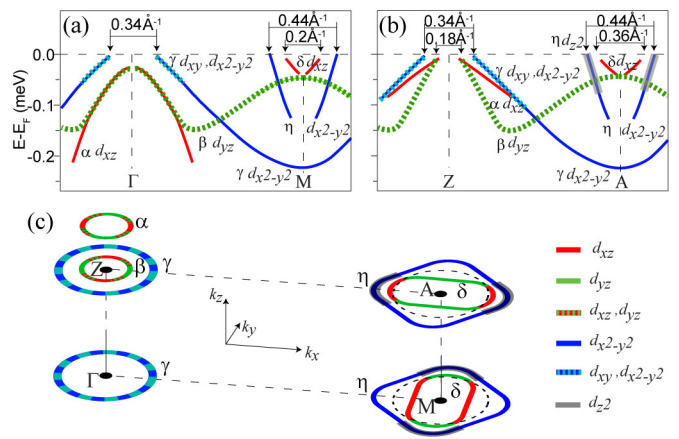


FIG. 8: (Color online) The summary of the orbital characters of low energy electronic structure. (a) and (b) The orbital characters of low energy electronic structure along  $\Gamma$ -M, and Z-A respectively. The solid and dashed lines represent the bands observed in the  $p$  and the  $s$  geometry respectively. (c) The illustration of the orbital characters on the Fermi surface sheets at  $\Gamma$ , M, Z, and A. The almost overlapping  $\alpha$  and  $\beta$  Fermi surface sheets at Z are separated for a better illustration. The black dashed circles around M and A are the duplicates of the  $\gamma$  Fermi surface sheets shifted from  $\Gamma$  and Z. The slight mixing between  $\delta$  and  $\beta$  near the zone corner is not shown though.

rectly, and electron-electron correlations may be strongly orbital dependent and result in the deviation from a simple local density approximation (LDA) calculation.

The pairing in the superconducting state can be strongly tied to the simultaneous existence of both Fermi surface sheets between the zone center and zone corner in iron-based superconductors. It has been suggested that the pairing is the strongest when the nesting condition between these two Fermi surface sheets are reached [24, 25]. However, in Fig. 8,  $\alpha$  and  $\beta$  show Fermi crossings with the distance about  $0.18\text{\AA}^{-1}$  at the Z point, which is still smaller than the  $0.2\text{\AA}^{-1}$  of the  $\delta$  band at the M point. Therefore, the  $\alpha$  and  $\beta$  bands do not nest well with the  $\delta$  band. The  $\gamma$  and  $\eta$  bands form one hole pocket and one electron pocket respectively with a cylinder-like shape in 3D Brillouin zone due to their 2D character and they are clearly not nested to each other as demonstrated by the black dashed circles in Fig. 8(c). If we include the  $k_z$  dependence, the size of the  $\delta$  electron pocket changes from  $0.2\text{\AA}^{-1}$  to  $0.36\text{\AA}^{-1}$ , passing the  $0.34\text{\AA}^{-1}$  of the  $\gamma$  bands. Therefore, the only possible nesting is between  $\gamma$  and  $\delta$  within a small  $k_z$  momentum window. It is hard to argue that this type of nesting can effectively enhance pairing since it takes place at a small region of  $k_z$ . In summary, our result does not support that the nesting condition (at least the strict nesting condition) plays a strong role in forming Cooper pairs.



## V. SUMMARY

To summarize, we have carried out a systematic investigation on orbital characters of  $\text{BaCo}_{0.15}\text{Fe}_{1.85}\text{As}_2$  and analyzed all the possible orbital characters of the multi-bands based on their strong polarization-dependent photoemission response. As recapitulated in Fig. 8, we found that although the main band structure is qualitatively consistent with the prediction of the present 2D band model, there are important differences between the current theories and our experimental results. The distribution of the  $d_{xz}$ ,  $d_{yz}$ , and  $d_{z^2}$  orbital character agree well with the theories, but the bands predicted to be  $d_{xy}$  orbital show a strong mixture with  $d_{x^2-y^2}$  orbital around the zone center and almost pure  $d_{x^2-y^2}$  orbital around the zone corner. The discrepancy between the calculated band structures and our experimental results suggests

that orbital dependent electron-electron correlations play an important role. We also study the 3D character of the electronic structure and show the strong  $k_z$  dependence of the Fermi surfaces and in-plane dispersion of certain bands, which proves that the 3D character is also strongly orbital dependent. Our results lay out a comprehensive picture of the orbital identities of the multi-band electronic structures, and provide explicit ingredients for constructing the theory of iron-based superconductors.

## VI. ACKNOWLEDGMENTS

This work was supported by the NSFC, MOE, MOST (National Basic Research Program), STCSM of China, the NSF of US under grant No. PHY-0603759, and HSRC under proposal 08-A-28.

- 
- [1] D. J. Singh and M. H. Du, Phys. Rev. Lett. **100**, 237003 (2008).
- [2] K. Kuroki, S. Onari, R. Arita, H. Usui, Y. Tanaka, H. Kontani and H. Aoki, Phys Rev Lett. **101**, 087004 (2008).
- [3] S. Graser, T. A. Maier, P. J. Hirschfeld and D. J. Scalapino, New J. Phys. **11**, 025016 (2009).
- [4] F. Wang, H. Zhai, and D. H. Lee, Phys. Rev. B **81**, 184512 (2010).
- [5] R. Thomale, C. Platt, W. Hanke and B. A. Bernevig, arXiv:1002.3599.
- [6] Y. Zhang, L. X. Yang, F. Chen, B. Zhou, X. F. Wang, X. H. Chen, M. Arita, K. Shimada, H. Namatame, M. Taniguchi, J. P. Hu, B. P. Xie and D. L. Feng, Phys. Rev. Lett. **105**, 117003 (2010).
- [7] D. Hsieh, Y. Xia, L. Wray, D. Qian, K. Gomes, A. Yazdani, G. F. Chen, J. L. Luo, N. L. Wang and M. Z. Hasan, arXiv:0812.2289[cond-mat.supr-con].
- [8] M. Yi, D. H. Lu, J. G. Analytis, J. H. Chu, S. K. Mo, R. H. He, R. G. Moore, X. J. Zhou, G. F. Chen, J. L. Luo, N. L. Wang, Z. Hussain, D. J. Singh, I. R. Fisher and Z. X. Shen, Phys. Rev. B **80**, 024515 (2009).
- [9] T. Shimojima, K. Ishizaka, Y. Ishida, N. Katayama, K. Ohgushi, T. Kiss, M. Okawa, T. Togashi, X. Y. Wang, C. T. Chen, S. Watanabe, R. Kadota, T. Oguchi, A. Chainani and S. Shin, Phys. Rev. Lett. **104**, 057002 (2010).
- [10] W. Malaeb, T. Yoshida, A. Fujimori, M. Kubota, K. Ono, K. Kihou, P. M. Shirage, H. Kito, A. Iyo, H. Eisaki, Y. Nakajima, T. Tamegai and R. Arita, J. Phys. Soc. Jpn. **78**, 123706 (2009).
- [11] S. V. Borisenko, V. B. Zabolotnyy, D. V. Evtushinsky, T. K. Kim, I. V. Morozov, A. N. Yaresko, A. A. Kordyuk, G. Behr, A. Vasiliev, R. Follath and B. Buchner, Phys. Rev. Lett. **105**, 067002 (2010).
- [12] S. Thirupathaiah, S. d. Jong, R. Ovsyannikov, H. A. Duerr, A. Varykhalov, R. Follath, Y. Huang, R. Huisman, M. S. Golden, Y.-Z. Zhang, H. O. Jeschke, R. Valenti, A. Erb, A. Gloskovskii and J. Fink, arXiv:0910.0147.
- [13] H. Q. Yuan, J. Singleton, F. F. Balakirev, S. A. Baily, G. F. Chen, J. L. Luo and N. L. Wang, Nature (London) **457**, 565 (2009).
- [14] P. Vilmercati, A. Fedorov, I. Vobornik, U. Manju, G. Panaccione, A. Goldoni, A. S. Sefat, M. A. McGuire, B. C. Sales, R. Jin, D. Mandrus, D. J. Singh and N. Mannella, Phys. Rev. B **79**, 220503(R) (2009).
- [15] S. Graser, A. F. Kemper, T. A. Maier, H.-P. Cheng, P. J. Hirschfeld and D. J. Scalapino, Phys. Rev. B **81**, 214503 (2010).
- [16] X. F. Wang, T. Wu, G. Wu, H. Chen, Y. L. Xie, J. J. Ying, Y. J. Yan, R. H. Liu and X. H. Chen, Phys. Rev. Lett. **102**, 117005 (2009).
- [17] L. X. Yang, Y. Zhang, H. W. Ou, J. F. Zhao, D. W. Shen, B. Zhou, J. Wei, F. Chen, M. Xu, C. He, Y. Chen, Z. D. Wang, X. F. Wang, T. Wu, G. Wu, X. H. Chen, M. Arita, K. Shimada, M. Taniguchi, Z. Y. Lu, T. Xiang and D. L. Feng, Phys. Rev. Lett. **102**, 107002 (2009).
- [18] Y. Zhang, J. Wei, H. W. Ou, J. F. Zhao, B. Zhou, F. Chen, M. Xu, C. He, G. Wu, H. Chen, M. Arita, K. Shimada, H. Namatame, M. Taniguchi, X. H. Chen and D. L. Feng, Phys. Rev. Lett. **102**, 127003 (2009).
- [19] M. Yi, D. H. Lu, J. G. Analytis, J. H. Chu, S. K. Mo, R. H. He, M. Hashimoto, R. G. Moore, I. I. Mazin, D. J. Singh, Z. Hussain, I. R. Fisher and Z. X. Shen, Phys. Rev. B **80**, 174510 (2009).
- [20] C. He, Y. Zhang, B. P. Xie, X. F. Wang, L. X. Yang, B. Zhou, F. Chen, M. Arita, K. Shimada, H. Namatame, M. Taniguchi, X. H. Chen, J. P. Hu and D. L. Feng, Phys. Rev. Lett. **105**, 117002 (2010).
- [21] A. Damascelli, Z. Hussain and Z.-X. Shen, Rev. Mod. Phys. **75**, 473 (2003).
- [22] D. L. Feng, C. Kim, H. Eisaki, D. H. Lu, A. Damascelli, K. M. Shen, F. Ronning, N. P. Armitage, N. Kaneko, M. Greven, J.-i. Shimoyama, K. Kishio, R. Yoshizaki, G. D. Gu and Z. X. Shen, Phys. Rev. B **65**, 220501(R) (2002).
- [23] D. J. Singh, Phys. Rev. B **78**, 094511 (2008).
- [24] H. Ding and et al., Europhys. Lett. **83**, 47001 (2008).
- [25] K. Terashima, Y. Sekiba, J. H. Bowen, K. Nakayama, T. Kawahara, T. Sato, P. Richard, Y.-M. Xu, L. J. Li, G. H. Cao, Z.-A. Xu, H. Ding and T. Takahashi, Proc. Natl. Acad. Sci. U.S.A. **106**, 7330 (2009).